Supporting Information for

HP-PbF_2-type $FeCl_2$ as a potential Cl-carrier in the deep Earth

Hongsheng Yuan[1*], Lianjie Man[1], Duck Young Kim[1], Dmitry Popov[2], Yue Meng[2], Eran Greenberg[3¶], Vitali Prakapenka[3], and Li Zhang[1*]

[1]Center for High Pressure Science and Technology Advanced Research (HPSTAR), Shanghai 201203, China

[2]HPCAT, X-ray Science Division, Argonne National Laboratory, Argonne, IL 60439, U.S.A.

[3]GeoSoilEnviroCARS, University of Chicago, Chicago, Illinois 60637, USA.

*Corresponding author: Hongsheng Yuan(hongsheng.yuan@hpstar.ac.cn), Li Zhang (zhangli@hpstar.ac.cn)

¶ Present address: Earn Greenberg: Applied Physics Division, Soreq Nuclear Research Center (SNRC), Yavne 81800, Israel.

Contents of this file

Text S1. Details of methods

Experimental

Synthesis of the En60 sample

MgO, Fe_2O_3, and SiO_2 with Mg: Fe: Si = 0.6: 0.4: 1 were mixed in an agate mortar with ethanol for more than two hours. The oxide mixtures were fired in a CO-CO_2 gas-mixing furnace at 1100 °C with oxygen fugacity of 1.8 log unit higher than Fe-FeO redox buffer to reduce the Fe^{3+} to Fe^{2+}. The as-prepared reduced sample was load into a graphite capsule. The En60 sample was then synthesized at 1.2 GPa and 1250 °C for 21 h in a piston cylinder press located at HPSTAR. The run product consists of pyroxene with 50–100 μm grain size and a minor amount of excessive SiO_2 as characterized by SEM. The chemical composition of the recovered sample is consistent with the starting material within the uncertainty of measurement as determined in an electron microprobe.

.

High *P-T* XRD

The Boehler-Almax bevelled diamond anvils with 150-μm culet size, rhenium (Re) gaskets and Mao-type symmetric DACs were used for high pressure generation. The pre-compressed α-FeO_2H disk was sandwiched between NaCl layers. For H_2O-bearing assemblies, a drop of distilled water was loaded and quickly sealed in the chamber; a small piece of Au (<5 μm in diameter) was loaded as the second pressure marker. The XRD experiments under high P-T conditions were performed in laser-heated DACs. The samples were heated using a double-sided laser heating technique (Prakapenka et al. 2008; Meng et al. 2015). The temperature was determined by fitting the visible portion of the black-body radiation from both sides of the heated sample to the Planck radiation function, with an estimated uncertainty of ±200 K throughout the heating. The XRD patterns were recorded using a MAR CCD area detector and CeO_2 or LaB_6 was used for the calibration of the sample-to-detector distances. The heating spot ranged from 15 to 35 μm in diameter, the X-ray spots was 3–5 μm in dimensions, and the sample was heated for duration of 2-10 minutes for each run. Changes of samples under high *P-T* conditions were monitored in-situ by powder XRD. A two-dimensional XRD scan was performed to record phase changes and distribution after *T* quench from each heating cycle. No correction has been made for thermal pressure during heating. The pressure after *T* quench is determined by the internally consistent pressure scales of NaCl or Au (Fei et al. 2007). Hundreds of submicron-sized single-crystal grains were simultaneously indexed using the multigrain XRD, where each individual grain can be treated as a single-crystal. The details of processing high-pressure multigrain data can be found elsewhere (Yuan and Zhang 2017; Zhang et al. 2019). Decompression XRD experiments with a wavelength of 0.6199 Å and a focused beam size of about 4 × 7 μm^2 were performed at beamline 15U1, Shanghai Synchrotron Radiation Facility, China. The Experimental conditions and results are summarized in Table S1.

TEM-EDS measurements

An FEI Versa-3D SEM coupled with a focused ion beam system was used to cut and lift out a thin cross-section from the heating center in the recovered sample. The thin section was polished to a thickness of approximately 60–100 nm using a focused Ga^+ ion beam.

Elemental mapping images were obtained using an FEI Talos F200X field emission TEM operating at 200 kV and equipped with a SuperX EDS system.

Calculations

In first-principle-based crystal structure searching, the computation was conducted using Vienna Ab Initio Software Package (VASP) (Kresse and Furthmüller 1996) based on density functional theory [DFT1, DFT2] (Hohenberg and Kohn 1964; Kohn and Sham 1965) with projected augmented wave method to GGA-PBE exchange-correlation functional (Perdew et al. 1996). The plane-wave cutoff is set to 300 eV and a 16×16×16 k points sampling is used. To treat correlation of d orbital of iron atoms properly, we employed DFT+U approach with a rotational invariant (Perdew et al. 1996). For the crystal structure searching, we used USPEX (Oganov et al. 2011) to find the ground state for each of the stoichiometries.

Text S2. Details of single-crystal refinements

A set of XRD patterns were collected for the Run ETR3 at the heating center position by rotating the DAC from –25 to 25° at steps of 0.25°. More than 500 grains were indexed consistent with the new cubic phase with a= 4.9779(6) Å at 100 GPa, and three of them were selected for the determination of the space group and structure. These three grains with different orientations were scaled and merged to increase coverage of the structure. The reflection conditions combined from three grains indicated the space group of $Pa\bar{3}$. Intensities of reflections from each grain have been calculated and compatibility between the three data sets has been checked by merging them using the XDS software (Kabsch 2010). The merged dataset of the three grains has provided satisfactory structural refinement for the new cubic phase. In total, 179 reflections have been combined from the three grains, and the refinement of the structure was performed against the resulting intensity data of 21 independent reflections using anisotropic thermal parameters. The structure was solved by the heavy atom method and refined using the SHELX package (Sheldrick 2007). Both the pyrite-type and HP-PdF_2-type structures process the identical space group of $Pa\bar{3}$, but they show different interanionic interactions. The $FeCl_2$ phase adopts the HP-PdF2-type structure due to the absence of the Cl–Cl covalent bond. The shortest Cl···Cl contact is ~2.564 Å.

Text S3. Electronic properties of HP-PdF_2-type $FeCl_2$

The electronic properties of compounds $M^{2+}X_2$ adopting the $Pa\bar{3}$ space group are largely governed by the X–X distance in the structures. The FeO_2 with the $Pa\bar{3}$ space group has been examined by theoretical simulations which found that the O–O dimer distance (~1.896 Å) is a key parameter governing the electronic properties in FeO_2 (Jang et al. 2017; Koemets et al. 2021). To understand the electronic structure of the HP-PdF_2-type $FeCl_2$, we employed DFT+U approach to properly treat d electrons of Fe atoms. We set the Hubbard U value to 2 eV as it is well applied to similar cases such as $CoCl_2$ (Kim et al. 2014) and FeS_2 (Lazić et al. 2013). It is worthy to note that standard DFT calculations lead to a metallic state. A previous study reported that the hexagonal $FeCl_2$ experienced a high-P-induced insulator-metal transition around 45 GPa under cold compression, which

leads to a first-order phase transition without a symmetry change (Rozenberg et al. 2009). Apparently, high *P*-*T* conditions alter both the crystal structure and electronic state of $FeCl_2$. Furthermore, recent calculations showed that at the inner core depth (corresponding to 360 GPa), the most stable iron-chloride compound is CsCl-type FeCl in the body-centered cubic Fe structure. The structure and stoichiometry of Fe-Cl compounds existing in the deep Earth will be upon further investigation within the realistic compositions.

Text S4. TEM-EDS analysis

As shown in Figure S3 and Table S2, except for the starting NaCl material, four different reaction products including (i) Fe-O-Cl, (ii) Si-O, (iii) Na,Fe-bearing silicate, and (iv) a possible partial melt were identified. Phase identification is discussed as follows.

(i) As the $FeCl_2$ compound is unstable and reacts with residual water in the sample chamber after recovery to ambient conditions, crystalline Fe-O-Cl compound (Figure S3g) other than $FeCl_2$ phase was observed. Also, the FIB cutting process may leads to a change in the $FeCl_2$-related quench product. This assignment is reasonable because the quenched product with the most Fe abundance in the phase assemblages should be derived from the high-*P* $FeCl_2$ phase.

(ii) For En60–H_2O and En60–H_2O–NaCl samples, the high-*P* XRD patterns were indexed as the phase assemblages of crystalline pPv + py and pPv + c-$FeCl_2$, respectively. There must be a silica-rich phase to meet the mass balance. However, no crystalline silica including $CaCl_2$-type, NiAs-type and α-PbO_2-type phase can be found in the high-*P* XRD patterns. Note that we did observe a large portion of silica-rich amorphous phase (Figure S3b and f) in the TEM-EDS mapping image in the quenched products of En60–H_2O–NaCl, and the amorphization of this silica-rich compound may be caused by the effect of water.

(iii) The Na,Fe-bearing silicate is the quenched compound of the high-*P* pPv phase on the basis of its stoichiometric composition (Table S2) and amorphous nature (Figure S3h) under ambient conditions.

(iv) The high-*P* XRD data provide information for the phase identification of crystalline phases. However, the principles of mass balance indicate that the reaction products should contain at least one more phase (probably amorphous) in each system: FeO_2H+NaCl → c-$FeCl_2$+ $Na_2FeCl_4OH_x$ + Na-rich phase (unknown); En60 + H_2O → pPv + py + silica-rich phase (unknown); En60 + H_2O + NaCl → Na,Fe-bearing pPv + c-$FeCl_2$ + silica-rich phase (supported by TEM-EDS) + Cl-bearing phase (supported by TEM-EDS). We think that the Cl-bearing phase is likely a partial melt because the high-*P* XRD patterns can be well explained by a mixture of c-$FeCl_2$ and pPv phases without observing other distinguishing diffractions. Note that the composition of this Cl-bearing phase cannot be unambiguously determined due to the complex sample environments, such as multiphase overlapping, possible reactions with residual water under ambient conditions and possible modification by the adjacent compounds in the FIB milling process.

References

Fei, Y., Ricolleau, A., Frank, M., Mibe, K., Shen, G., and Prakapenka, V. (2007) Toward an internally consistent pressure scale. Proceedings of the National Academy of Sciences, 104, 9182–9186.

Hohenberg, P., and Kohn, W. (1964) Inhomogeneous Electron Gas. Physical Review, 136, B864–B871.

Jang, B.G., Kim, D.Y., and Shim, J.H. (2017) Metal-insulator transition and the role of electron correlation in FeO_2. Physical Review B, 95, 075144.

Kabsch, W. (2010) Xds. Acta Crystallographica Section D: Biological Crystallography, 66, 125–132.

Kim, B., Kim, K., and Min, B.I. (2014) Universal metastability of the low-spin state in Co^{2+} systems: Non-Mott type pressure-induced spin-state transition in $CoCl_2$. Physical Review B - Condensed Matter and Materials Physics, 89, 115131.

Koemets, E., Leonov, I., Bykov, M., Bykova, E., Chariton, S., Aprilis, G., Fedotenko, T., Clément, S., Rouquette, J., Haines, J., and others (2021) Revealing the Complex Nature of Bonding in the Binary High-Pressure Compound FeO_2. Physical Review Letters, 126, 106001.

Kohn, W., and Sham, L.J. (1965) Self-Consistent Equations Including Exchange and Correlation Effects. Physical Review, 140, A1133–A1138.

Kresse, G., and Furthmüller, J. (1996) Efficiency of ab-initio total energy calculations for metals and semiconductors using a plane-wave basis set. Computational Materials Science, 6, 15–50.

Lazić, P., Armiento, R., Herbert, F.W., Chakraborty, R., Sun, R., Chan, M.K.Y., Hartman, K., Buonassisi, T., Yildiz, B., and Ceder, G. (2013) Low intensity conduction states in FeS_2: Implications for absorption, open-circuit voltage and surface recombination. Journal of Physics Condensed Matter, 25.

Meng, Y., Hrubiak, R., Rod, E., Boehler, R., and Shen, G. (2015) New developments in laser-heated diamond anvil cell with in situ synchrotron x-ray diffraction at High Pressure Collaborative Access Team. Review of Scientific Instruments, 86, 072201.

Oganov, A.R., Lyakhov, A.O., and Valle, M. (2011) How evolutionary crystal structure prediction works-and why. Accounts of Chemical Research, 44, 227–237.

Perdew, J.P., Burke, K., and Ernzerhof, M. (1996) Generalized gradient approximation made simple. Physical Review Letters, 77, 3865–3868.

Prakapenka, V.B., Kubo, A., Kuznetsov, A., Laskin, A., Shkurikhin, O., Dera, P., Rivers, M.L., and Sutton, S.R. (2008) Advanced flat top laser heating system for high pressure research at GSECARS: Application to the melting behavior of germanium. In High Pressure Research Vol. 28, pp. 225–235.

Rozenberg, G.K., Pasternak, M.P., Gorodetsky, P., Xu, W.M., Dubrovinsky, L.S., Le Bihan, T., and Taylor, R.D. (2009) Pressure-induced structural, electronic, and magnetic phase transitions in $FeCl_2$ studied by x-ray diffraction and resistivity measurements. Physical Review B, 79, 214105.

Sheldrick, G.M. (2007) A short history of SHELX. Acta Crystallographica Section A: Foundations of Crystallography, 64, 112–122.

Yuan, H., and Zhang, L. (2017) In situ determination of crystal structure and chemistry of minerals at Earth's deep lower mantle conditions. Matter and Radiation at Extremes, 2, 117–128.

Zhang, L., Yuan, H., Meng, Y., and Mao, H. (2019) Development of High-Pressure Multigrain X-Ray Diffraction for Exploring the Earth's Interior. Engineering, 5, 441–447.

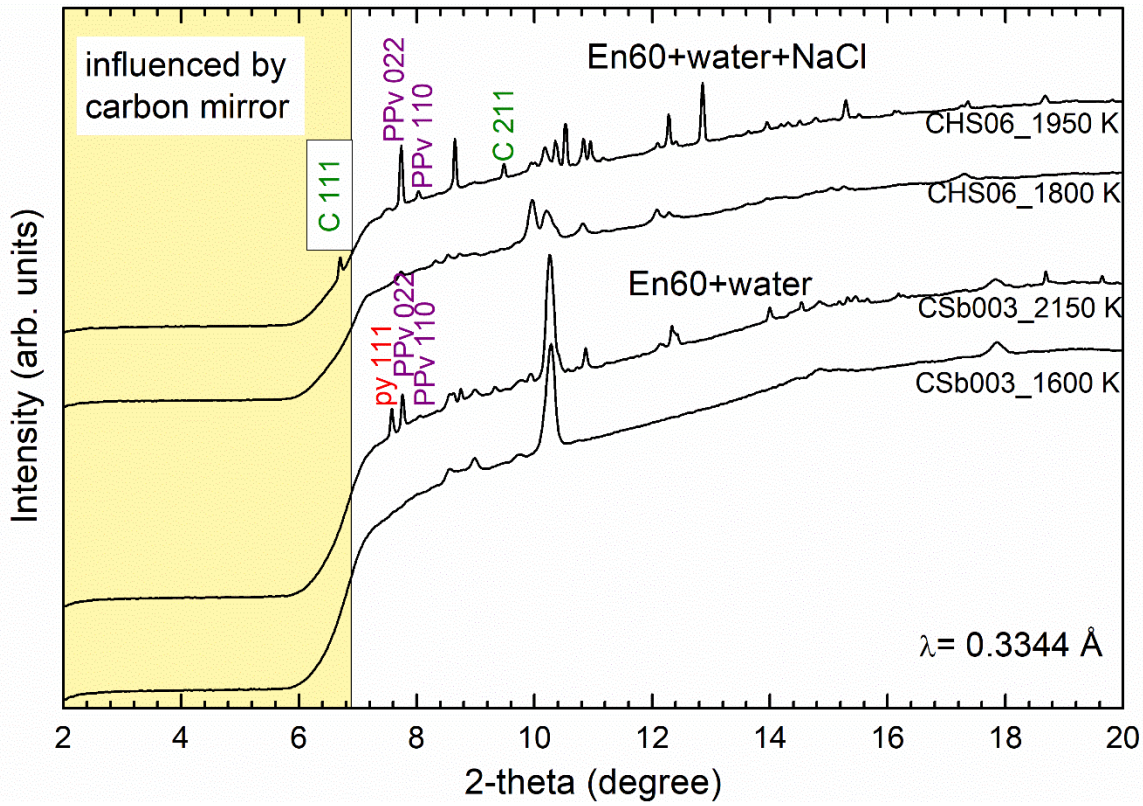

Figure S1. High *P-T* XRD patterns for Runs CHS06 (top) and CSb003 (bottom). The characteristic diffractions are marked. The py-phase and C phase are observed at high T and Room T (Fig. 1 in the main text), indicating that these two phases are not quenched phases from melts. The yellow part is marked as diffraction portion influenced by the carbon mirror in the laser heating system.

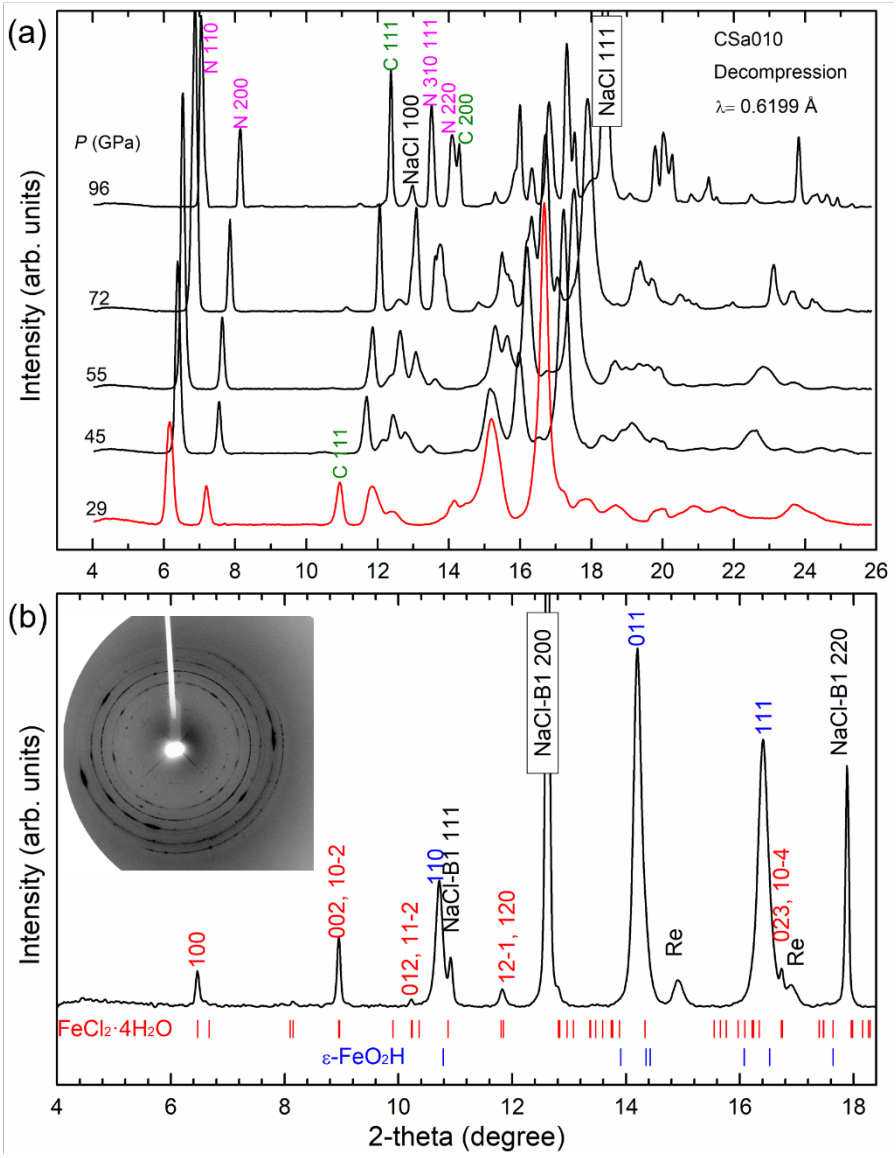

Figure S2 Room *T* XRD patterns of the sample synthesized from Run CSa010 at (a) high and (b) ambient pressures during decompression. The characteristic diffractions of both $Na_2FeCl_4OH_x$ and c-$FeCl_2$ phases can be well tracked from 96 to 29 GPa during decompression at room *T*. When the sample was decompressed to ambient conditions, the $Na_2FeCl_4OH_x$ and c-$FeCl_2$ phases could not be observed. The ambient XRD pattern can be indexed by the coexisting $FeCl_2{\cdot}4H_2O$ and ε-FeO_2H phases. The peak positions of these two phases, the $FeCl_2{\cdot}4H_2O$ phase (space group: $P2_1/C$) with a= 5.885(3), b= 7.180(6), c= 8.514(4), β= 111.09(2)° and the ε-FeO_2H phase (space group: *Pnnm*) with a = 4.937 Å, b = 4.432 Å, c = 2.994 Å, are indicated with red and blue ticks, respectively. Inset of panel b shows the XRD image for the quenched sample. Experiments were performed with X-ray wavelength of 0.6199 Å at 15U1, SSRF.

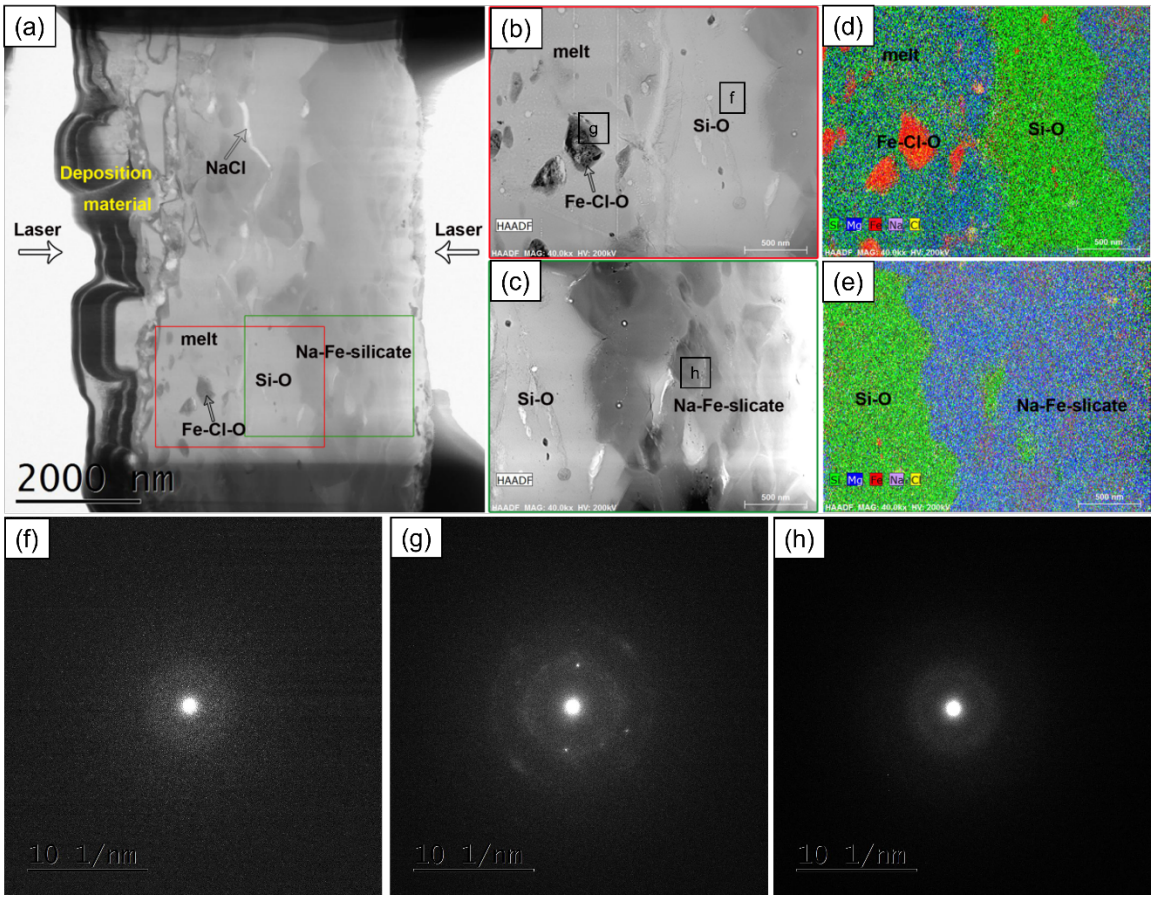

Figure S3. Elemental mapping images for the recovered sample. (a) HAADF image of the recovered sample. The enlarged enlarged image of box red (b) and green (c) in panel a. Overlapped Si+Mg+Fe+Na+Cl mapping images (d) and (e). According to the texture and chemical composition (Table S3), four individual parts (Fe-Cl-O: the $FeCl_2$ compound reacting with water and air after quench; Si-O: SiO_2-rich phase; Na-Fe silicate: the high-pressure pPv phase after quench; a possible partial melt) in the quenched sample were identified. Selected area electron diffraction patterns (f), (g) and (f) for Si-O, Fe-Cl-O and Na-Fe silicate, respectively, as marked in panels b and c.

Table S1. Experimental conditions.

Run no.	Starting materials	*P* scale,[#] *a* (Å)	*P* (GPa)	*T* (K)	t[*] (mins)
CHS06	En60–NaCl–H_2O	Au, 3.696(1)	108(2)	1950(200)	5
CSb003	En60–H_2O	Au, 3.709(1)	115(2)	2150(200)	5
ETR3	α-FeOOH–NaCl	NaCl-B2, 2.734(1)	100(2)	1700(200)	2
				2000(200)	2
CSa010	α-FeOOH–NaCl	NaCl-B2, 2.743(1)	96(2)	2050(200)	10

[#] The pressure is calculated after *T* quench; [*]t, heating duration.

Table S2. Comparison of the refined structure from our experiment (Run ETR3) for the HP-PdF_2-type $FeCl_2$ at 100(2) GPa with the theoretically predicted structure at 100 GPa.

Experiment	*a*= 4.980(5) Å				
Atom	Site	*x*	*y*	*z*	U_{eq}
Fe	4a	0	0	0	0.018(3)
Cl	8c	0.3514(4)	0.3514(4)	0.3514(4)	0.016(3)
Measured/independent/free reflections 179/21/3			Completeness 95%		
R/R_{free} 0.040/0.089			R_{int} 0.083		
Theory	*a*= 4.9489 Å				
Atom	Site	*x*	*y*	*z*	
Fe	4a	0	0	0	
Cl	8c	0.35175	0.35175	0.35175	

Table S3. Compositional results of the concerned phases.

Phases	Melt[#]	σ	SiO_2-rich	σ	Fe-Cl-O[#]	σ	Silicate(pPv)	σ
atom%								
O	69.5	0.7	69.1	0.3	47.9	1.7	63.3	0.7
Si	19.0	0.7	28.2	0.9	1.5	0.4	18.2	0.3
Mg	8.7	0.9	0.3	0.1	1.4	0.7	11.8	0.4
Fe	0.8	0.2	1.9	0.9	35.5	0.4	4.5	0.2
Na	0.0	0.0	0.0	0.0	3.5	0.5	2.2	0.2
Cl	2.1	0.3	0.5	0.0	10.2	0.5	0.0	0.0
Total	100.0		100.0		100.0		100.0	

Data in the column of "σ" indicate the relevant uncertainties.

[#] The composition of the Cl-bearing partial melt and Fe-Cl-O compound may be ambiguous.